

On-orbit calibration of soft X-ray detector on Chang'E-2 satellite^{*}

XIAO Hong(肖虹) PENG Wen-Xi(彭文溪)¹⁾ WANG Huan-Yu(王焕玉)¹⁾
 CUI Xing-Zhu(崔兴柱) GUO Dong-Ya(郭东亚)

Institute of High Energy Physics, CAS, Beijing 100049, China

Abstract: The X-ray spectrometer is one of the satellite payloads on the Chang'E-2 satellite. The soft X-ray detector is one of the devices on the X-ray spectrometer, designed to detect the major rock-forming elements within the 0.5–10 keV range on the lunar surface. In this paper, energy linearity and energy resolution calibration is done using a weak ⁵⁵Fe source. Temperature and time effects are found not to give a large error. The total uncertainty of calibration is estimated to be within 5% after correction.

Key words: SXD, calibration, on-orbit

PACS: 95.55.Pe, 95.85.Nv **DOI:** 10.1088/1674-1137/39/10/106002

1 Introduction

Following the precursor Chang'E-1 (CE-1) satellite, a second Chinese lunar spacecraft, Chang'E-2 (CE-2), was launched on October 1, 2010. The CE-2 spacecraft resembles the CE-1 mission but with improved instrument performance. With the onboard instruments, a huge amount of lunar scientific data was obtained successfully during the CE-2 mission.

The X-ray spectrometer (XRS) is one of the scientific payloads on CE-2. The XRS is composed of a lunar X-ray detector (LXD) and solar X-ray monitor (SXM), as shown in Fig. 1(a). The SXM is mainly used to monitor the solar X-ray flux and energy spectrum. The LXD

(layout shown in Fig. 1(b)) comprises two perpendicular arrays. Each array includes two soft X-ray detectors (SXD) which are used to detect fluorescent X-rays within 1–10 keV on the lunar surface, and eight hard X-ray detectors (HXD), which are used to detect X-rays on the lunar surface within the energy range 25–60 keV. Si-PIN X-ray sensors are used in each detector unit, which are equipped with bias circuits, charge sensitive preamplifiers and main amplifier circuits, while each detector unit works independently from the other. In order to monitor the performance variation of SXD, a weak ⁵⁵Fe source ($\sim 1 \mu\text{Ci}$) was glued inside the collimator close to the Be window, also as shown in Fig. 1(b). Table 1 shows the specification of the SXDs [1].

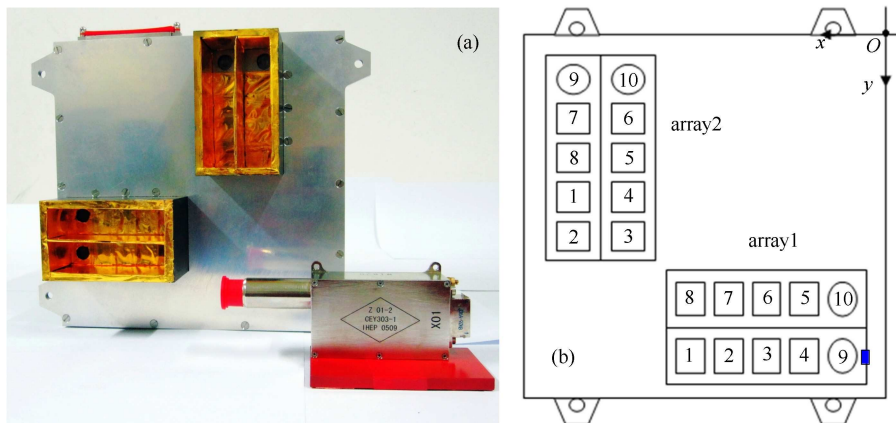


Fig. 1. (color online) (a) X-ray spectrometer on CE-2(left: lunar X-ray detector (LXD); right: solar X-ray monitor (SXM)); (b) LXD structure (circle is SXD, rectangle is HXD, blue rectangle is ⁵⁵Fe source).

Received 2 February 2015

^{*} Supported by National Science Foundation of Ministry of Education

1) E-mail: pengwx@ihep.ac.cn

©2015 Chinese Physical Society and the Institute of High Energy Physics of the Chinese Academy of Sciences and the Institute of Modern Physics of the Chinese Academy of Sciences and IOP Publishing Ltd

Table 1. SXD specifications.

parameters	values
component	soft X-ray detector(SXD)
objective	lunar X-ray fluorescence
detector	Si-PIN*4 chips
filter	12.5 μm beryllium
energy range	0.5–10 keV
effective area	1 cm^2
energy resolution	300 eV@5.9 keV
ADC	10 bits

The scientific goal of the XRS is to obtain the abundance distribution of the major rock-forming elements (Mg, Al, Si, Ca, Ti, Fe and etc.) on the lunar surface. Precise results can be obtained by accumulating the data in each area of the lunar surface to get enough statistics, but first energy calibration should be done. Energy calibration generally includes calibration of energy linearity and energy resolution. The result of on-orbit calibration using ^{55}Fe source will be introduced in this article [2].

2 On-orbit calibration of energy linearity and resolution calibration

The CE-2 satellite went into circumlunar orbit on October 2nd, 2010. The X-ray spectrometer data was transferred to the ground-based system from October 15th, 2010. About 7 months' data was obtained for this analysis, including data on longitude, latitude, height, quality state and so on. In this section, we select good quality events from Oct. 18th, 2010 to Oct. 20th, 2010 for the on-orbit calibration analysis, when solar flare level was higher than C5 (solar flares higher than $5 \times 10^{-6} \text{ W/m}^2$ between 1 and 8 angstroms detected by NOAA satellites) [3].

X-rays lose energy in the sensitive medium of the detector. The detection of incident photon energy is actually the detection of photon energy lost in the detector. For X-ray photons which deposit all their energy in the detector, the amplitude of the electronic signal represents the incident X-ray energy. This allows the relation between energy and channel to be directly obtained, so then the channel-count spectrum can be converted to an energy-count spectrum. In short, the principle of energy linearity calibration is calibrating the correlation between different X-ray energies and the channel of the electronic signal.

Normally, for a silicon X-ray detector system, the peak pulse height has a linear relationship with the incident energy of the X-ray, the fitting equation used in calibration of the energy-channel curve is

$$E = K \times ch + \Delta E = K_1 \times ch + C_1, \quad (1)$$

where ch is the channel, E is the incident X-ray energy, K is the slope, and ΔE is the intercept [4].

In the energy spectrum, the full energy peaks of rock-forming elements on the lunar surface (Mg, Al, Si, Ca, Ti, Fe etc.) and Mn excited by the ^{55}Fe source can be obtained. Considering the energy resolution and line intensity, the full energy peaks of Ca, Mn and Fe are chosen to be fitted with a Gaussian to do the energy linearity and resolution calibration. The fitting result of one detector (SXD Array1-9) is shown in Fig. 2.

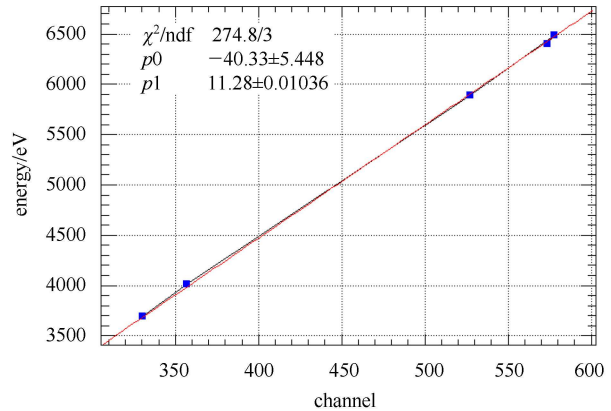


Fig. 2. (color online) Energy linearity calibration of SXD array 1–9, showing the correlation between channel and energy.

The energy resolution of a detector is usually evaluated by the FWHM of the full energy peak. The full energy spectrum of monoenergetic X-rays in an X-ray spectrometer is a Gaussian spectrum from theoretical estimation and calibration experiment analysis. The energy spectrum of the Si-PIN detector can therefore be fitted with a Gaussian distribution.

The energy resolution of the X-ray spectrometer can be influenced by two factors. One is the statistical fluctuation of random processes in ionization, and the other is noise generated by the electronics system.

The first factor (ΔE_1) is related to the incident X-ray energy, and the relationship can be described by the function $\Delta E_1 = (KE)^{1/2}$.

The second factor (ΔE_2) has nothing to do with the incident X-ray energy. According to the error propagation equation, the FWHM can be expressed as:

$$FWHM = \sqrt{\Delta E_1^2 + \Delta E_2^2} = \sqrt{K \times E + \Delta E^2}, \quad (2)$$

$$FWHM^2 = K \times E + \Delta E^2 = K_2 \times E + C_2. \quad (3)$$

Equation (3) is used in fitting the energy resolution curve.

Figure 3 is the fitting result of energy resolution calibration showing the correlation between energy and FWHM.

Energy linearity and energy resolution calibration of the soft X-ray detectors are calibrated independently, with the detailed fit result shown in Table 2.

Table 2. On-orbit calibration of energy peak and energy resolution.

fit result	E vs. channel		$FWHM^2$ vs. E	
	K_1	C_1	K_2	C_2
array1-9	11.28 ± 0.01	-40.33 ± 5.45	0.0221 ± 0.0021	680.50 ± 10.19
array2-9	10.97 ± 0.003	-22.86 ± 1.42	0.0386 ± 0.0083	637.70 ± 28.94

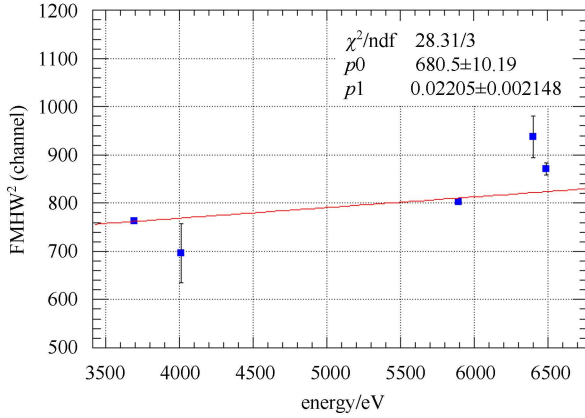


Fig. 3. (color online) Energy resolution calibration result plot for SXD array 1-9.

3 On-orbit calibration using radioactive sources and calibration uncertainties

Because of the different environment in space, the calibration results will be different. There are two factors affecting the on-orbit performance of the SXD: in the short term, the performance changes with the orbit; and in the long term degradation caused by space radiation damage.

The main mechanisms of space radiation damage to silicon detectors are total dose effects and displacement effects. Both effects will cause an increase in the dark current and decrease in the energy resolution. In a circumlunar orbit, space radiation is mainly from galactic cosmic rays, energetic solar particles and high energy electrons.

Through on-orbit calibration data with the weak ^{55}Fe radioactive source (which only affects SXD array 1-9), the orbit-variation and time-variation of SXD performance are analyzed in this section.

Due to there being active temperature control systems, signal fluctuation of the SXDs is almost unaffected by the outside temperature, but the electronic noise increases as the temperature increases. The energy resolution of the detector will deteriorate as the temperature increases.

There are three thermal sensors (TMR130, TMR146 and TMR147) on the X-ray spectrometer, which can detect the temperature of the solar X-ray monitor, lunar x-ray detector and electronics crate respectively. However, the temperature of TMR146 is the temperature of the X-ray spectrometer shell, and there is an unknown

temperature gradient in the vacuum environment, so it does not give the exact temperature of the temperature sensitive device. The parameter of the back-end electronics though will change over time. So the temperature of TMR146 is just taken as a reference.

Because CE-2 is a polar orbit satellite, the orbital period is about 127 minutes, and there is no big change in longitude in every cycle (only about 1°). We then find there is a positive relation between the temperature of TMR146 and the latitude; as an example, about 6 hours of data from Oct 20th, 2010 are shown in Fig. 4 for comparison. We select the data in a fixed latitude range, and then divide the data into several longitude bins to see the change [5].

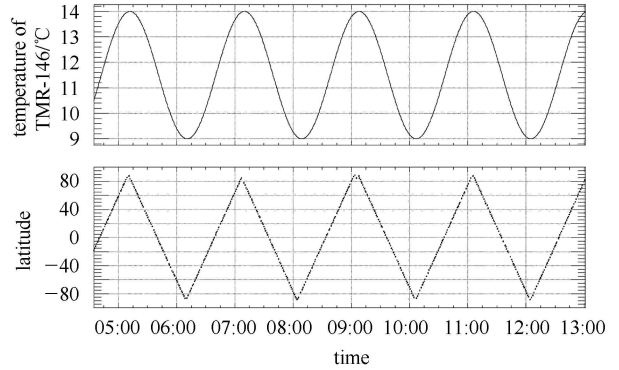


Fig. 4. Relationship between temperature and latitude on Oct 20th, 2010 (top: temperature of TMR-146 vs. time bottom: latitude vs. time).

Powerful solar flares will affect the calibration result, so we first select the data with solar flare level lower than C5. Because temperature is related to longitude and latitude, small $30^\circ \times 30^\circ$ grids (longitude 12 bins, latitude 6 bins) are analyzed to eliminate the temperature effect, assuming there is negligible change in temperature in any given grid. The time effect is first checked, with the Mn peak in every single grid in every month separately fitted as shown in Fig. 5(a). The relation between calibration and time is shown in detail in Fig. 5(b). The plot shows six months' data, with every point the result of one month's data fit, there appears to be no regular trend in the figure. Because of the different environment, the average energy resolution (about 28 channels) on-orbit became a little larger than the ground-based result (about 26 channels), as we expected. The latitude is then fixed in the range 60° to 90° to see the calibration change while the longitude changes, as shown in Fig. 5(c). The

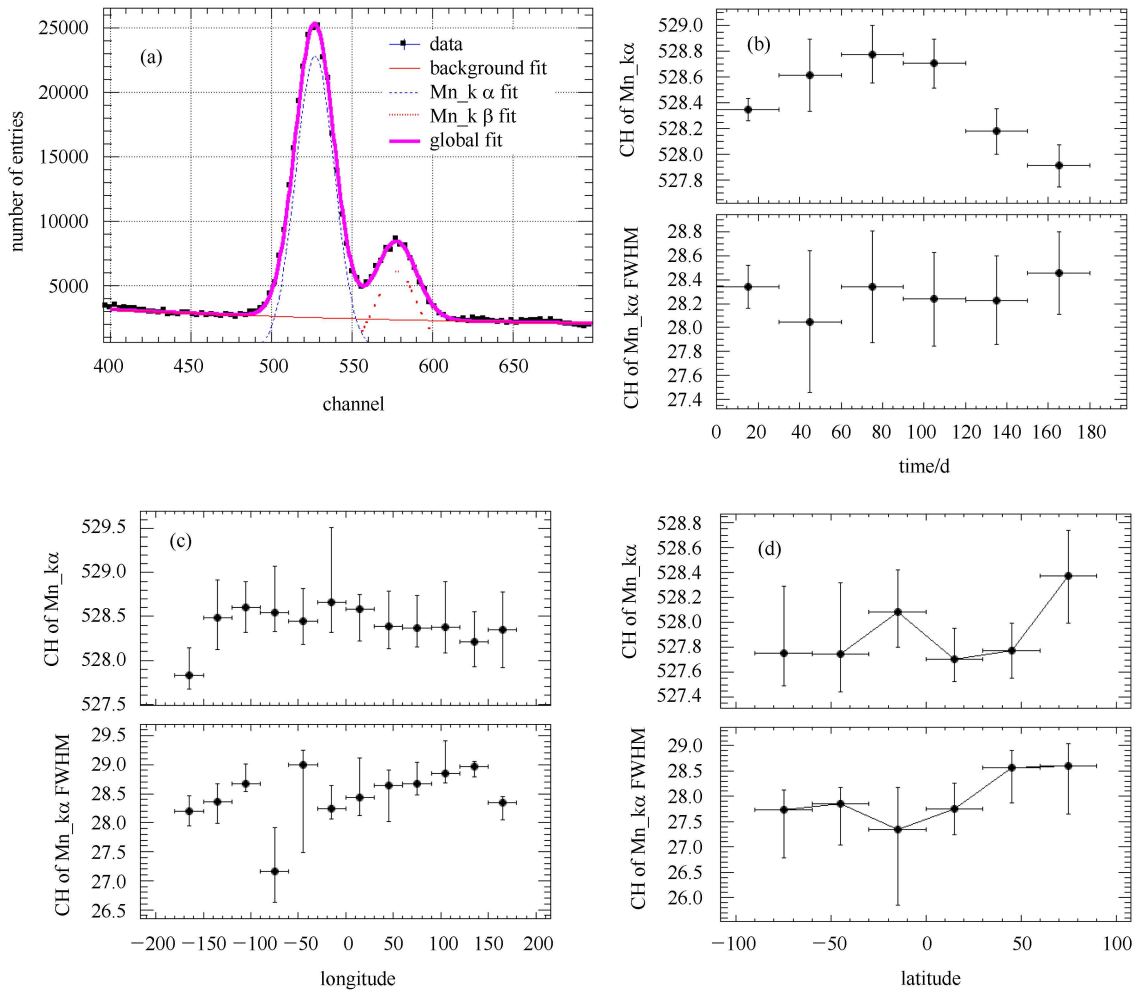


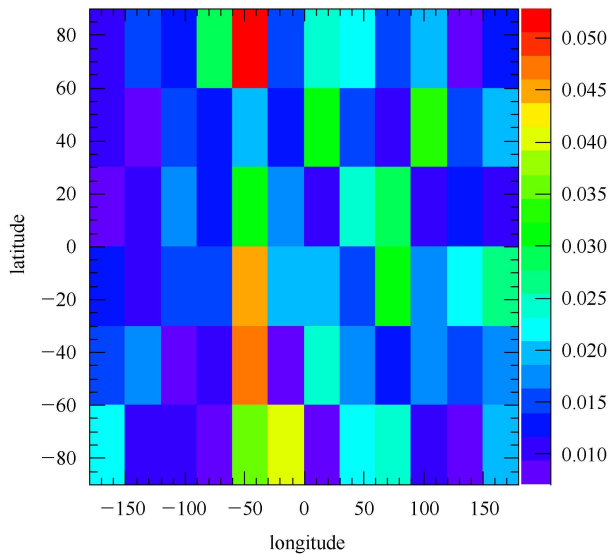
Fig. 5. (color online) (a) ^{55}Fe full energy peak fit example in one of the $30^\circ \times 30^\circ$ grids for one month, (b) Calibration result change with time (top: peak position, bottom: FWHM, unit: channel), (c) Calibration result change with longitude for latitude range 60° to 90° (top: peak position, bottom: FWHM, unit: channel), (d) Calibration result change with latitude for longitude range 0° to 30° (top: peak position, bottom: FWHM, unit: channel).

Table 3. First month ^{55}Fe peak position calibration result (unit: channel).

longitude latitude	-90° – -60°	-60° – -30°	-30° – 0°	0° – 30°	30° – 60°	60° – 90°
-180° – -150°	527.732 ± 0.086	527.766 ± 0.085	528.008 ± 0.087	527.383 ± 0.082	527.495 ± 0.085	527.830 ± 0.090
-150° – -120°	527.749 ± 0.086	527.879 ± 0.084	527.748 ± 0.081	527.616 ± 0.082	527.868 ± 0.084	528.486 ± 0.087
-120° – -90°	528.184 ± 0.078	528.012 ± 0.078	527.967 ± 0.085	528.020 ± 0.080	528.430 ± 0.088	528.607 ± 0.089
-90° – -60°	528.289 ± 0.082	528.207 ± 0.087	528.200 ± 0.087	528.080 ± 0.090	528.592 ± 0.091	528.539 ± 0.095
-60° – -30°	528.047 ± 0.103	527.952 ± 0.108	527.665 ± 0.108	527.555 ± 0.107	528.384 ± 0.114	528.446 ± 0.115
-30° – 0°	527.848 ± 0.106	527.946 ± 0.106	527.894 ± 0.102	528.134 ± 0.101	528.294 ± 0.101	528.660 ± 0.099
0° – 30°	528.164 ± 0.093	527.997 ± 0.088	528.418 ± 0.087	528.168 ± 0.088	528.286 ± 0.087	528.582 ± 0.094
30° – 60°	527.867 ± 0.088	528.220 ± 0.086	527.690 ± 0.088	527.742 ± 0.088	528.277 ± 0.090	528.391 ± 0.091
60° – 90°	527.775 ± 0.083	527.784 ± 0.083	528.081 ± 0.084	527.690 ± 0.086	527.745 ± 0.84	528.365 ± 0.090
90° – 120°	527.901 ± 0.085	527.718 ± 0.089	527.594 ± 0.092	527.652 ± 0.089	527.882 ± 0.088	528.381 ± 0.086
120° – -150°	527.752 ± 0.085	527.801 ± 0.082	527.628 ± 0.084	528.204 ± 0.083	527.731 ± 0.082	528.207 ± 0.084
150° – -180°	527.828 ± 0.084	527.912 ± 0.082	527.694 ± 0.082	527.971 ± 0.085	527.983 ± 0.084	528.350 ± 0.086

Table 4. Sixth month ^{55}Fe peak position calibration result (unit: channel).

longitude latitude	-90° – -60°	-60° – -30°	-30° – 0°	0° – 30°	30° – 60°	60° – 90°
-180° – -150°	527.361 ± 0.169	527.503 ± 0.161	527.826 ± 0.167	527.122 ± 0.157	527.297 ± 0.163	527.672 ± 0.174
-150° – -120°	527.608 ± 0.171	527.748 ± 0.169	527.574 ± 0.161	527.495 ± 0.163	527.885 ± 0.166	528.119 ± 0.174
-120° – -90°	527.990 ± 0.152	527.932 ± 0.152	527.736 ± 0.162	527.813 ± 0.158	528.144 ± 0.165	528.316 ± 0.168
-90° – -60°	528.251 ± 0.160	528.143 ± 0.169	528.075 ± 0.168	527.971 ± 0.175	528.311 ± 0.170	528.331 ± 0.179
-60° – -30°	527.970 ± 0.191	527.778 ± 0.195	527.551 ± 0.198	527.564 ± 0.198	528.156 ± 0.206	528.205 ± 0.212
-30° – 0°	527.593 ± 0.199	527.852 ± 0.198	527.723 ± 0.196	527.927 ± 0.194	528.120 ± 0.193	528.316 ± 0.191
0° – 30°	527.795 ± 0.171	527.944 ± 0.166	528.288 ± 0.166	528.143 ± 0.169	528.173 ± 0.163	528.527 ± 0.173
30° – 60°	527.728 ± 0.167	528.062 ± 0.163	527.560 ± 0.165	527.858 ± 0.167	528.187 ± 0.166	528.195 ± 0.167
60° – 90°	527.559 ± 0.157	527.642 ± 0.158	527.952 ± 0.158	527.654 ± 0.161	527.696 ± 0.156	528.233 ± 0.167
90° – 120°	527.621 ± 0.159	527.416 ± 0.168	527.370 ± 0.173	527.469 ± 0.167	527.621 ± 0.167	528.087 ± 0.165
120° – -150°	527.568 ± 0.157	527.435 ± 0.151	527.488 ± 0.155	528.010 ± 0.152	527.592 ± 0.152	528.041 ± 0.158
150° – -180°	527.471 ± 0.157	527.746 ± 0.155	527.552 ± 0.153	527.892 ± 0.157	527.807 ± 0.157	527.914 ± 0.165

Fig. 6. (color online) Global calibration error in a $10^\circ \times 10^\circ$ grid on the lunar surface.

upper limit of each point indicates the maximum value in that longitude bin over 6 months, while the lower limit gives the minimum value, and the point position is the fit result of the whole 6 months. The longitude was then fixed in the range 0° to 30° to see the calibration change while the latitude changes, as shown in Fig. 5(d). The detailed results for the peak position in each grid for the first and sixth months are shown in Tables 3, 4.

We assume that the peak position and FMHW calibr-

ation result in every month in every grid are almost unaffected by time. In order to get calibration error on the lunar surface, the full energy peak position should be corrected with these parameters so as not to add extra uncertainty. The efficiency detection result is supposed to take a negligible uncertainty. The systematic error of the FMHW in every grid is thought to be mainly taken by time effect. The total error is shown in Fig. 6, including both statistical error and systematic error, the element distribution error in the grid can be estimated from this figure. We can conclude that the global calibration uncertainty was within 5% during the mission.

4 Conclusion

In order to satisfy the scientific goals of the CE-2 project, calibration of the soft X-ray detector has been successfully designed and accomplished. On-orbit calibration was used to check the performance of each of the soft X-ray detectors. Energy linearity and energy resolution were calibrated using a ^{55}Fe source. The temperature and time effect were also taken account of, with no major change found for either effect. The overall calibration uncertainty is estimated to be within 5%.

We thank the National Astronomical Observatories of the Chinese Academy of Sciences (NAOC) for providing the on-orbit data. We also thank the reviewers for improving the paper.

References

- 1 Peng Wen-Xi et al. Chinese Physics C, 2009, **819**: 33
- 2 ZUO Wei et al. Chin. J. Geochem., 2014, **33**: 024–044
- 3 <http://spaceweather.com/glossary/flareclasses.html>
- 4 Grande M et al. Planetary and Space Science, 2009, **57**: 717–724
- 5 Stefanie L Lawson et al. Journal of Geophysical Research, VOL. 105, No. E2, PAGES 4273–4290, February 25, 2000